Journal of Magnetic Resonance 290 (2018) 29–37

Contents lists available at ScienceDirect

Journal of Magnetic Resonance

journal homepage: www.elsevier.com/locate/jmr

# Considering low-rank, sparse and gas-inflow effects constraints for accelerated pulmonary dynamic hyperpolarized $^{129}$Xe MRI

Sa Xiao [a,b,1], He Deng [a,b,1], Caohui Duan [a,b], Junshuai Xie [a,b], Huiting Zhang [a], Xianping Sun [a,b], Chaohui Ye [a,b], Xin Zhou [a,b,*]

[a] State Key Laboratory of Magnetic Resonance and Atomic and Molecular Physics, National Center for Magnetic Resonance in Wuhan, Wuhan Institute of Physics and Mathematics, Chinese Academy of Sciences, Wuhan 430071, PR China
[b] University of Chinese Academy of Sciences, Beijing 100049, PR China

ARTICLE INFO

*Article history:*
Received 11 January 2018
Revised 2 March 2018
Accepted 5 March 2018
Available online 8 March 2018

*Keywords:*
Dynamic MRI
Hyperpolarized $^{129}$Xe
Pulmonary inspiration
Compressed sensing
Low-rank
Sparse
Gas-inflow effects

ABSTRACT

Dynamic hyperpolarized (HP) $^{129}$Xe MRI is able to visualize the process of lung ventilation, which potentially provides unique information about lung physiology and pathophysiology. However, the longitudinal magnetization of HP $^{129}$Xe is nonrenewable, making it difficult to achieve high image quality while maintaining high temporal-spatial resolution in the pulmonary dynamic MRI. In this paper, we propose a new accelerated dynamic HP $^{129}$Xe MRI scheme incorporating the low-rank, sparse and gas-inflow effects (L + S + G) constraints. According to the gas-inflow effects of HP gas during the lung inspiratory process, a variable-flip-angle (VFA) strategy is designed to compensate for the rapid attenuation of the magnetization. After undersampling k-space data, an effective reconstruction algorithm considering the low-rank, sparse and gas-inflow effects constraints is developed to reconstruct dynamic MR images. In this way, the temporal and spatial resolution of dynamic MR images is improved and the artifacts are lessened. Simulation and *in vivo* experiments implemented on the phantom and healthy volunteers demonstrate that the proposed method is not only feasible and effective to compensate for the decay of the magnetization, but also has a significant improvement compared with the conventional reconstruction algorithms (*P*-values are less than 0.05). This confirms the superior performance of the proposed designs and their ability to maintain high quality and temporal-spatial resolution.



## 1. Introduction

Magnetic resonance imaging (MRI) is widely used for diagnostic and therapeutic purposes because of its clinical safety and superior soft tissue contrast to conventional imaging methods (such as computed tomography, X-ray). Although conventional $^{1}$H MRI has been applied for most human organ systems, it is rarely utilized for the lungs due to the very low density of $^{1}$H in the lung tissue. Through the spin-exchange optical pumping (SEOP) technique, hyperpolarized (HP) gas (such as $^{3}$He and $^{129}$Xe) MRI makes imaging of both pulmonary ventilation [1] and diffusion [2] feasible. This can provide the structural and functional information about the lungs, such as the microstructure, gas–gas and/or gas-blood exchange functions [3–5]. Accordingly, HP gas MRI offers great potential in the early detection of lung diseases, for example chronic obstructive pulmonary disease (COPD), emphysema and cystic fibrosis [2,6].

Many studies using HP gas MRI (such as the ventilation imaging [5], dissolved-phase $^{129}$Xe MRI [7], diffusion-weighted imaging [8]) acquire lung images during the time interval of the breath-hold (denoted as static HP gas MRI). However, such static HP gas MRI does not visualize the dynamics of the pulmonary structure and/or function during the ventilation process, which potentially masks some abnormal regions, such as collateral ventilation and pulmonary air leaks [9,10]. It is known that the dynamic imaging of ventilation process has great potential to provide unique information about lung physiology and pathophysiology, which is valuable for clinical diagnosis and prognosis evaluation. Therefore, these findings warrant the development of dynamic HP gas MRI.

In 1996, MacFall et al. first obtained dynamic images of human lungs using a fast gradient echo sequence, at a temporal resolution of 1800 ms [11]. In 2000, Gierada et al. utilized echo-planar imaging with a temporal resolution of 40 ms in dynamic HP gas MRI of the lungs, but the spatial resolution was seriously constrained [12]. In the same year, Viallon et al. performed dynamic HP gas MRI with

* Corresponding author at: Wuhan Institute of Physics and Mathematics, Chinese Academy of Sciences, 30 West Xiaohongshan, Wuhan, PR China.
*E-mail address:* xinzhou@wipm.ac.cn (X. Zhou).
[1] Authors who contributed equally to this work.

https://doi.org/10.1016/j.jmr.2018.03.003
1090-7807/

interleaved spiral cine sequences [13]. Although the acquired images had a high temporal and spatial resolution, the temporal resolution was pseudo due to the combination with the sliding window reconstruction [14]. In 2001, Salerno et al. performed dynamic HP gas MRI in humans using interleaved spiral pulse sequences, which visualized regional ventilatory patterns with high temporal and spatial resolution [15]. However, large number of interleaves in spiral pulse sequences limited the SNR of the image [16,17]. In 2003, Wild et al. demonstrated the feasibility of the radial projection method in dynamic HP gas MRI using sliding window reconstruction [18]. High temporal and spatial resolution can be achieved in this work, but with a loss of SNR and increased radial streaking artifacts [14]. In 2008, Holmes et al. presented 3D dynamic imaging of the lung using a multiple echo vastly undersampled isotropic projection reconstruction sequence [19]. This method resulted in high spatial resolution, but blurred the image details and produced streaking artifacts. It can be found that there exists a trade-off between image quality and temporal-spatial resolution for dynamic HP gas MRI because of the nonrenewable properties of HP longitudinal magnetization. This necessitates an effective dynamic HP gas MRI technique, aiming to simultaneously achieve high image quality and temporal-spatial resolution.

To reduce the disadvantages due to the nonrenewable longitudinal magnetization in dynamic HP gas MRI, we adopt compressed sensing (CS) strategy in this paper because CS can recover signals and images accurately using significantly fewer measurements than the number required by traditional Nyquist sampling [20–22]. CS has been widely applied to accelerate the MRI acquisition by undersampling k-space data [23–25]. Moreover, CS has also successfully been used in the dynamic MRI, such as the dynamic total variation [26], blind CS [27], and low-rank plus sparse matrix decomposition (L + S) methods [28]. However, in dynamic HP gas MRI, when HP gas is inhaled into the lung, considerable effects on the MR signals are generated (i.e., gas-inflow effects), which trigger complicate changes of signal intensity [16,29,30]. These changes will bring some unfavorable factors (such as noise and artifacts) in both sampling and reconstruction processes, limiting the image quality. Consequently, the gas-inflow effects should be considered in the pulmonary dynamic HP gas MRI.

In this work, we develop a new variable-flip-angle (VFA) scheme considering the gas-inflow effects to compensate for the decay of HP longitudinal magnetization, and then design an effective reconstruction algorithm incorporating the low-rank (L), sparse (S) and gas-inflow effects (G) constraints. This aims to acquire pulmonary dynamic images with high quality and temporal-spatial resolution. Meanwhile, HP $^{129}$Xe is preferred in this work due to its lower cost and wider availability in regional lung function assessment compared with HP $^{3}$He [30,31].

## 2. Methods

### 2.1. Data acquisition

In static HP gas MRI with a constant-flip-angle (CFA) scheme, the HP gas signal intensity after the $n$-th radiofrequency (RF) excitation is described as follows if the longitudinal relaxation time ($T_1$) is ignored [16,32],

$$S_1(n) = M_0(\cos\theta)^{n-1}\sin\theta,\ M_0 = \mu\cdot V, \tag{1}$$

where $\theta$ is the flip angle, $M_0$ is the initial longitudinal magnetization, $\mu$ is a constant relating to the initial polarization and spin density of HP gas, and $V$ is the volume of inhaled HP gas. Eq. (1) shows the decay of longitudinal magnetization of HP gas due to the RF excitations, which suggests that a smooth k-space filter is imposed on the data and results in blurring the image details [14]. VFA schemes were developed to compensate for the losses of magnetization by gradually increasing flip angles [33–35]. However, the gas-inflow effects potentially limit the performance of conventional VFA schemes in pulmonary dynamic HP gas MRI. The inhaled HP gas will bring in more available magnetization during the dynamic imaging, which may increase the weight of high frequency part of k-space data. Consequently, a new VFA scheme is developed that does not only compensate for the depolarization caused by the preceding RF pulses (as is the case with conventional VFA schemes) but also takes into account the continuous gas inflow. Moreover, undersampling strategy is adopted to accelerate the imaging speed of dynamic HP gas MRI. Fig. 1 shows the timing diagram of the data acquisition process, where $M$, $N$ and $K$ are the number of phase encoding ($k_y$), frequency encoding ($k_x$) and frames, $a$ is the acceleration factor (AF), and $\theta_n$, $n = 1,\ldots,(M/a)\times K$ are the variable flip angles. Variable density undersampling patterns along the phase-encoding direction are generated using a Monte Carlo algorithm and extended to minimize the peak interference of the transform point spread function (TPSF) [23].

To obtain favorable variable flip angles, we introduce a concept of average signal intensity (ASI). Assuming that $S_2(n)$ and $V(n)$ denote the HP gas signal intensity and the volume of inhaled HP gas after the $n$-th excitation in dynamic MRI, the ASI of HP gas $[S_p(n)]$ is

$$S_p(n) = S_2(n)/V(n),\ n = 1,\ldots,(M/a)\times K, \tag{2}$$

Moreover, we assume that the inhaled flow rate ($r$) is a constant. Then, $V(n)$ is equal to the product of $r$ and inspiratory time $T$ ($T = n\cdot$TR, where TR is the pulse repetition time). Owing to the continuous inspiration, $V(n+1) = V(n) + r\cdot$TR. Accordingly, the signal intensity after $(n+1)$-th excitation is

$$S_2(n+1) = \frac{S_2(n)}{\sin\theta_n}\cdot\cos\theta_n\cdot\sin\theta_{n+1} + \mu\cdot r\cdot \mathrm{TR}\cdot\sin\theta_{n+1}, \tag{3}$$

where $\theta_n$ and $\theta_{n+1}$ are the flip angles used in the $n$-th and $(n+1)$-th excitations. In this way, $S_2(n)$ can be considered as the sum of the signal intensity of the HP gas inhaled in each pulse TR, that is

$$S_2(n) = r\cdot\mathrm{TR}\cdot\mu\cdot\sin\theta_n\cdot\left(1+\sum_{i=1}^{n-1}\prod_{j=i}^{n-1}\cos\theta_j\right), \tag{4}$$

Thus, the ASI after the $n$-th excitation can be expressed as

$$S_p(n) = S_2(n)/V(n) = \frac{1}{n}\cdot\mu\cdot\sin\theta_n\cdot\left(1+\sum_{i=1}^{n-1}\prod_{j=1}^{n-1}\cos\theta_j\right), \tag{5}$$

The gas-inflow effects make the decay of the magnetization more complex (16), which results in difficulties in depicting the dynamics of the HP gas signal. It can be seen from Eq. (5) that with a constant flip angle the ASI is monotonically decreased with the excitation number, which indicates that the ASI can reflect the filter imposed on the k-space data. Therefore, it may be a feasible way to compensate for the filter by maintaining a constant ASI. We intend to compensate for the decay by maintaining a constant ASI, namely, $S_p(n) = S_p(n\text{-}1)$, $n = 2,\ldots,(M/a)\times K$. Therefore, the flip angles used in the proposed scheme are [See Appendix A],

$$\theta_n = \arcsin\left\{\frac{n\cdot\sin\theta_1}{(n-1)\cdot\sin\theta_1\cdot A(n)+1}\right\},\ \text{where } A(n) = \frac{\cos\theta_{n-1}}{\sin\theta_{n-1}}. \tag{6}$$

If the initial flip angle $\theta_1$ is known under a given $n$ (or if the $\theta_n$ is defined), a series of flip angles are determined. For example, when the excitation number is 960 and the initial flip angle is 2.42°, $\theta_{960} = 31.81°$.

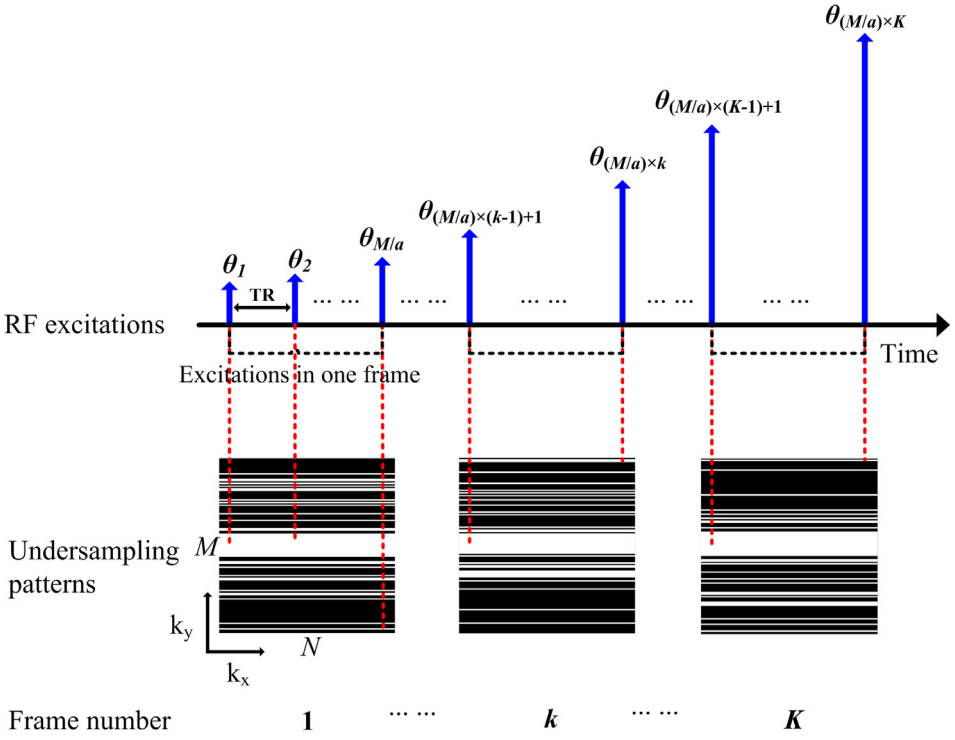


**Fig. 1.** Timing diagram of the data acquisition process.

### 2.2. Image reconstruction

After the acquisition of undersampled data, it is important to effectively reconstruct MR images. Dynamic MR images can be regarded as a superposition of background and dynamic components, which have low-rank and transform sparse properties [28]. Moreover, two characteristics of signal variations in dynamic pulmonary inspiration images should be considered because of the gas-inflow effects. One is that the signal region in the lung gradually expands with the increase of inhaled HP gas volume. The other characteristic is that the signal intensity of the signal region increases to a steady state in a short time, and then becomes reasonably stable over the remainder of the acquisition [29]. Accordingly, a reconstruction strategy (L + S+G) incorporating the low-rank, sparse and gas-inflow effects constraints is proposed in this paper. The reconstruction objective function is designed as

$$\arg\min_{L,S}\left\{\frac{1}{2}||E(L+S)-d||_2^2+\lambda_G||\Psi(L+S)\circ(L+S)||_2^2+\lambda_L||L||_*+\lambda_S||TS||_1\right\}, \tag{7}$$

where $E$ is the transformation matrix of the image to undersampled k-space data, $L$ is the low-rank part of the image, $S$ is the sparse part, $d$ is the undersampled k-space data, $\Psi$ represents the differences between the adjacent frames, $\circ$ is the element-wise product operator, $T$ is a sparse transform matrix, and $\lambda_G$, $\lambda_L$ and $\lambda_S$ are the regularization parameters to balance the gas-inflow effects, low-rank part and sparse part of the image, respectively. $L$ and $S$ are the space–time matrices, where each column is a temporal frame. Specifically, both the decrease in the signal region of the lung and the fluctuation of the signal intensity that is far greater than zero will sharply increase the value of the second term in the proposed objective function. In this way, characteristics caused by the gas-inflow effects are constrained. Since the proposed objective function is a convex optimization problem, a number of numerical algorithms can be used to solve it. An algorithm based on the combination of singular value thresholding and iterative soft thresholding [28] is used here because this algorithm has a good convergence and can guarantee optimal solutions of the $L$ and $S$. The iterations are terminated when the relative change in the solution is less than $10^{-5}$. The regularization parameters are empirically chosen based on visual inspection, which leads to good empirical results.

### 2.3. Experiments

Informed consents were obtained from all subjects. All experiments were performed in accordance with the guidelines and regulations provided and approved by the Institutional Review Board of Wuhan Institute of Physics and Mathematics (WIPM), Chinese Academy of Sciences (CAS).

The experiments were performed on a 1.5 Tesla whole-body MRI scanner (Avanto, Siemens Medical Solutions). Enriched xenon was polarized by the SEOP technique with a “freeze-out” accumulation procedure using a cold finger and home-built xenon polarizer. The available polarization of xenon in the Tedlar bag was approximately 20%. Volumes of 500 mL HP xenon and 500 mL medical grade $N_2$ were mixed into the 1 L gas mixture. All subjects were trained to breathe in the gas mixture from their functional residual capacity (FRC) at a constant rate (100–150 mL $s^{-1}$).

In simulation experiments performed on a phantom, we measured the HP $^{129}$Xe signal intensity using the proposed VFA (initial flip angle $\theta_1 = 9.38°$), conventional VFA (initial flip angle $\theta_1 = 7.18°$) (33), and CFA ($\theta_c = 12°$) schemes. The total excitation number was 64, and ASI was calculated through Eq. (2). A home-built 8-leg birdcage RF coil tuned to $^{129}$Xe frequency was used. During the experiments, the HP $^{129}$Xe was delivered into a Tedlar bag with a syringe at a constant flow rate, and the tidal volume per imaging was 70 mL. After receiving the NMR FIDs, a dephase gradient was applied in the read orientation at the end of each repetition. Then the NMR FIDs were transformed to complex Lorentzian spectra by Fourier transform, followed by phase correction. Spectral peaks were at 0 ppm in the absorption Lorentzian. We chose the integral

range from −15 ppm to 15 ppm in the absorption Lorentzian line shape as the signal intensity.

Another simulation experiment was performed on a healthy volunteer. A home-built transmit-receive vest RF coil was used. Pulmonary dynamic HP $^{129}$Xe MR data was fully acquired with the proposed VFA (initial flip angle $\theta_1 = 2.42°$), conventional VFA (initial flip angle $\theta_1 = 1.85°$) and CFA ($\theta_c = 7°$) schemes. The imaging parameters of the 2D FLASH sequence were as follows: the matrix size = 64 × 64, slice thickness = 20 cm, frame number = 15, echo time (TE) = 5.0 ms, TR = 10.5 ms, field of view (FOV) = 384 × 384 mm$^2$, bandwidth (BW) = 10.24 kHz, and centric encoding in the phase encoding direction. Then, fully sampled (FS) data was undersampled with an AF of 3 for reconstruction. We used the mean absolute error (MAE) [36], structural similarity index (SSIM) [37], quality index based on local variance (QILV) [38] and contrast-to-noise ratio (CNR) [39] to demonstrate the reconstruction performance of the proposed L + S + G algorithm. Among them, MAE gave an absolute error measure, SSIM gave an estimate of the structure missing, QILV indicated some blurring and CNR provided the quality of the contrast.

Six healthy volunteers were enrolled for the dynamic HP $^{129}$Xe MRI experiments *in vivo* with the proposed VFA scheme. A home-built transmit-receive vest RF coil was used. The imaging parameters were as follows: the matrix size = 128 × 128, AF = 3, and initial flip angle $\theta_1 = 3°$. The other imaging parameters were identical to those in the simulation experiment performed on a healthy volunteer. Then the HP $^{129}$Xe MR images were reconstructed with different algorithms. Because the calculation of MAE, SSIM and QILV requires a reference image, which was unavailable in the experiments *in vivo*, we adopted the CNR to evaluate the image quality. CNR compares a measure of the activation fluctuations to the noise, which is sensitive to the variation of the signal and background noise (35). To further test the feasibility to measure the dynamics of HP $^{129}$Xe signal with the proposed method, signal-frame curves are calculated.

To evaluate the performance of the proposed reconstruction algorithm, we selected some widely used techniques as baseline methods for comparison, such as the sparse representation-based compressed sensing (SRCS) [23] and L + S [28] algorithms. The two-tailed *t* test was used to investigate whether there were significant differences in the results of L + S + G, SRCS and L + S algorithms. All groups of MR data were processed in MATLAB (MathWorks, Natick, MA).

## 3. Experimental results

### 3.1. Simulation

Phantom results are shown in Fig. 2, including the theoretical ASI data and experimental values obtained using the proposed VFA, conventional VFA and CFA schemes. The ASI values through the proposed VFA scheme are constant over all the excitation number. However, the ASI values obtained using the conventional VFA scheme monotonically increase with the excitation number, and those through the CFA scheme monotonically decrease. Moreover, we use R-Squared to evaluate the goodness-of-fit. The R-Squared for the proposed VFA, conventional VFA, and CFA scheme are 0.98, 0.99 and 0.98, respectively. This suggests that the experimental values are very close to the theoretical values and the proposed VFA scheme can compensate for the ASI decay effectively.

For the healthy volunteer under fully sampling strategy, Fig. 3a–c show the experimental results of the 10th frame obtained using the proposed VFA, conventional VFA and CFA excitation schemes, respectively. It can be seen that the noise in Fig. 3a is lower than that in Fig. 3b. In addition, the details in Fig. 3a are sharper than that in Fig. 3c (denoted by the green rectangles). This demonstrates the efficacy of the proposed VFA scheme for compensating for magnetization decay.

As for the reconstruction performance of the proposed algorithm, Fig. 4a–d shows the 15th frame of FS images and corresponding reconstruction results using the SRCS, L + S and L + S + G. Considerable artifacts are found in the reconstructed SRCS image (indicated by white arrows). The image obtained using L + S algorithm has some losses of structures and details due to the smooth-

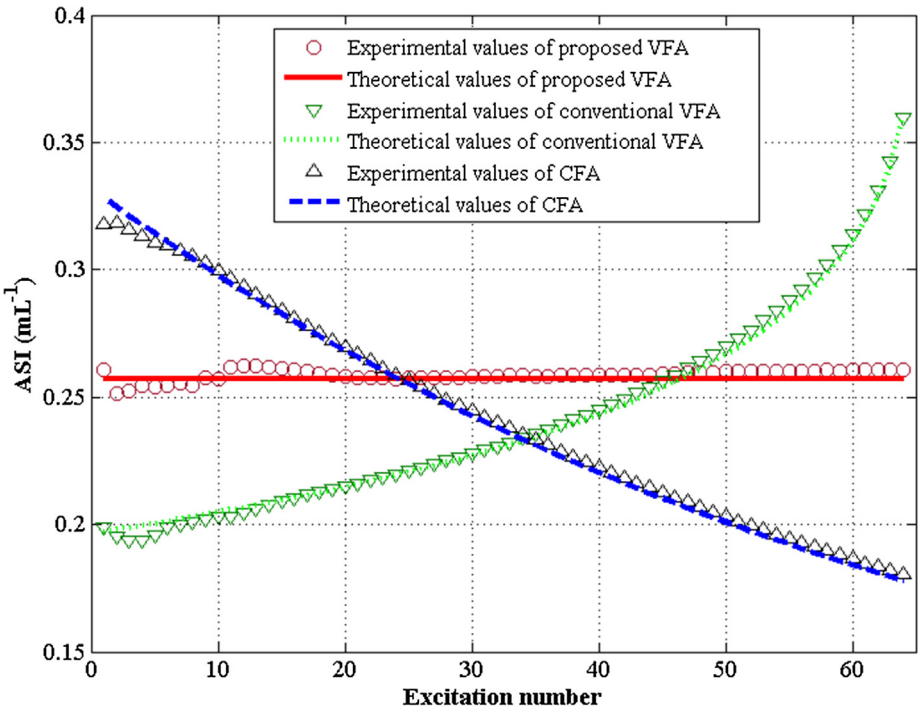


**Fig. 2.** The theoretical ASI data and experimental values obtained using the proposed VFA, conventional VFA and CFA schemes.

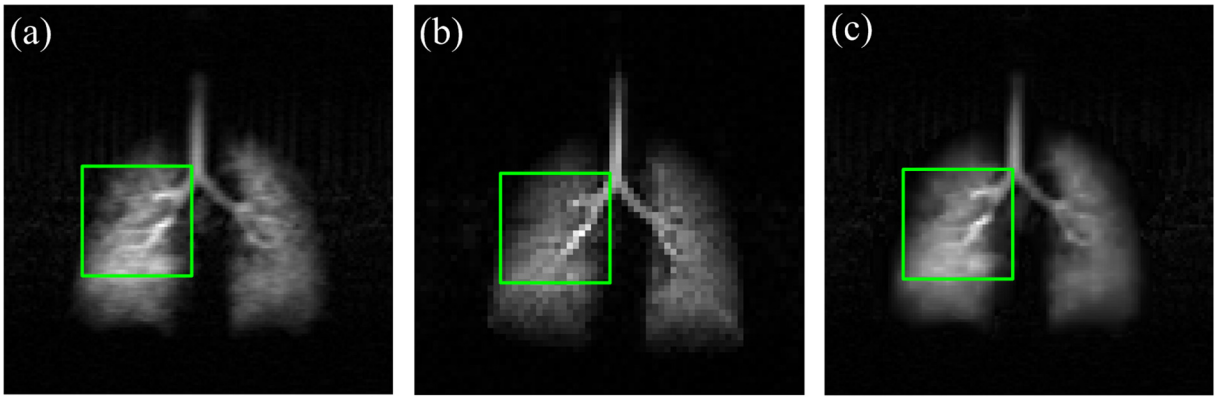


**Fig. 3.** Experimental results of the 10th frame obtained through the (a) proposed VFA, (c) conventional VFA, and (c) CFA schemes.

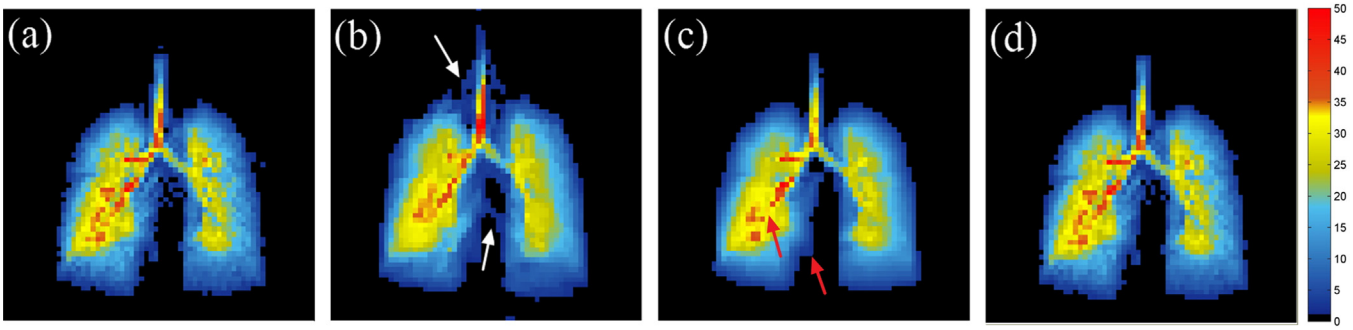


**Fig. 4.** Reconstruction results of the 15th frame of simulation dynamic HP $^{129}$Xe MR images. (a) The FS image. (b) Images reconstructed by using SRCS, (c) L + S and (d) L + S + G algorithm.

**Table 1**
Comparisons of the MAE, SSIM, QILV and CNR in simulation experiments obtained using different algorithms (*I* denotes the improvement of L + S + G algorithm compared with other two classic reconstruction algorithms).

| | MAE (%) | SSIM | QILV | CNR |
|---|---|---|---|---|
| SRCS | 2.66 ± 0.94 | 0.74 ± 0.07 | 0.89 ± 0.06 | 19.94 ± 2.79 |
| L + S | 1.94 ± 0.92 | 0.77 ± 0.06 | 0.91 ± 0.09 | 23.97 ± 1.25 |
| L + S+G | 1.35 ± 0.96 | 0.94 ± 0.09 | 0.96 ± 0.02 | 31.15 ± 4.10 |
| $P_{L+S+G\_vs\_SRCS}$ | <0.0001 | <0.0001 | <0.0001 | <0.0001 |
| $I_{L+S+G\_vs\_SRCS}$ | 49.25% | 27.03% | 7.87% | 56.22% |
| $P_{L+S+G\_vs\_L+S}$ | 0.0451 | <0.0001 | 0.0323 | <0.0001 |
| $I_{L+S+G\_vs\_L+S}$ | 30.41% | 22.08% | 5.49% | 29.90% |

ing effect of the total variation constraints (indicated by the red arrow). However, the artifacts are effectively suppressed and the details are better preserved in L + S + G images.

Table 1 lists the MAE, SSIM, QILV and CNR of reconstructed images using different reconstruction algorithms. The mean and standard deviation are calculated over the 15 frames and that the statistically significant difference was also assessed over those 15 different values. As demonstrated in Table 1, the results obtained using L + S + G scheme show statistically significant improvement compared with that using the SRCS ($P < 0.05$) and L + S methods ($P < 0.05$). The MAE of the results using the L + S + G algorithm decrease by 30.41% compared with that using the L + S, and even more compared with that using the SRCS. The SSIM, QILV and CNR in the results using the L + S + G algorithm increase by 22.08%, 5.49% and 29.90% compared with that using L + S, and even more compared with that using SRCS. These results corroborate the qualitative findings in Fig. 3.

To further demonstrated the effect of the proposed VFA scheme on the reconstruction, undersampled data of the new VFA, conventional VFA and CFA schemes are reconstructed using L + S + G algorithm. Fig. 5a–c shows the reconstruction results of the undersampled data. It can be seen that the Fig. 5a has better performance both in noise suppression and detail preservation than Fig. 5b and c. Table 2 lists the MAE, SSIM, QILV and CNR of reconstructed images using different data acquisition schemes. The mean and standard deviation are calculated over the 15 frames. These results of the proposed VFA scheme show significant improvement compared with the conventional VFA and CFA schemes, demonstrating the favorable effects of the proposed VFA scheme on image reconstruction.

### 3.2. In vivo prospective acquisitions

Fig. 6 shows the fifteen frames of the dynamic pulmonary inspiration images of a healthy volunteer acquired using the proposed schemes. It can be seen that a good visualization of gas dynamics is provided with the AF of 3, and the inspiratory process is clearly visualized in this volunteer over the 6.67 s duration of the experiment. These frames depict the filling of the main trachea to the

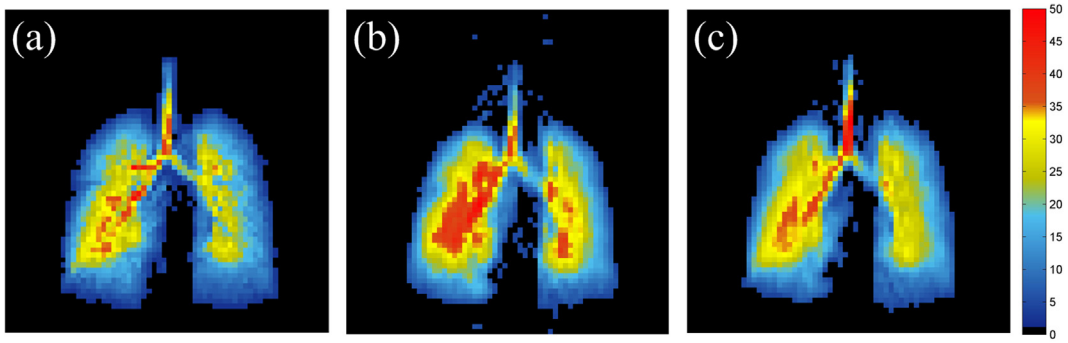


**Fig. 5.** Reconstruction results of the undersampled data acquired using (a) proposed VFA scheme, (b) conventional VFA scheme and (c) CFA scheme.

**Table 2**
Comparisons of the MAE, SSIM, QILV and CNR in simulation experiments obtained using the proposed VFA scheme, conventional VFA scheme and CFA scheme. (*I* denotes the improvement of L + S + G algorithm compared with other two classic reconstruction algorithms, pVFA denotes the proposed VFA scheme, cVFA denotes the conventional VFA scheme).

| | MAE (%) | SSIM | QILV | CNR |
|---|---|---|---|---|
| Proposed VFA | 1.35 ± 0.96 | 0.94 ± 0.09 | 0.96 ± 0.02 | 31.15 ± 4.10 |
| Conventional VFA | 1.73 ± 0.46 | 0.72 ± 0.07 | 0.91 ± 0.08 | 26.33 ± 4.13 |
| CFA | 1.82 ± 0.59 | 0.76 ± 0.05 | 0.90 ± 0.08 | 24.40 ± 3.50 |
| $P_{pVFA\_vs\_cVFA}$ | 0.1228 | <0.0001 | 0.0096 | <0.0001 |
| $I_{pVFA\_vs\_cVFA}$ | 21.97% | 30.56% | 5.49% | 18.31% |
| $P_{pVFA\_vs\_CFA}$ | 0.0479 | <0.0001 | 0.0078 | <0.0001 |
| $I_{pVFA\_vs\_CFA}$ | 25.82% | 23.68% | 6.67% | 27.66% |

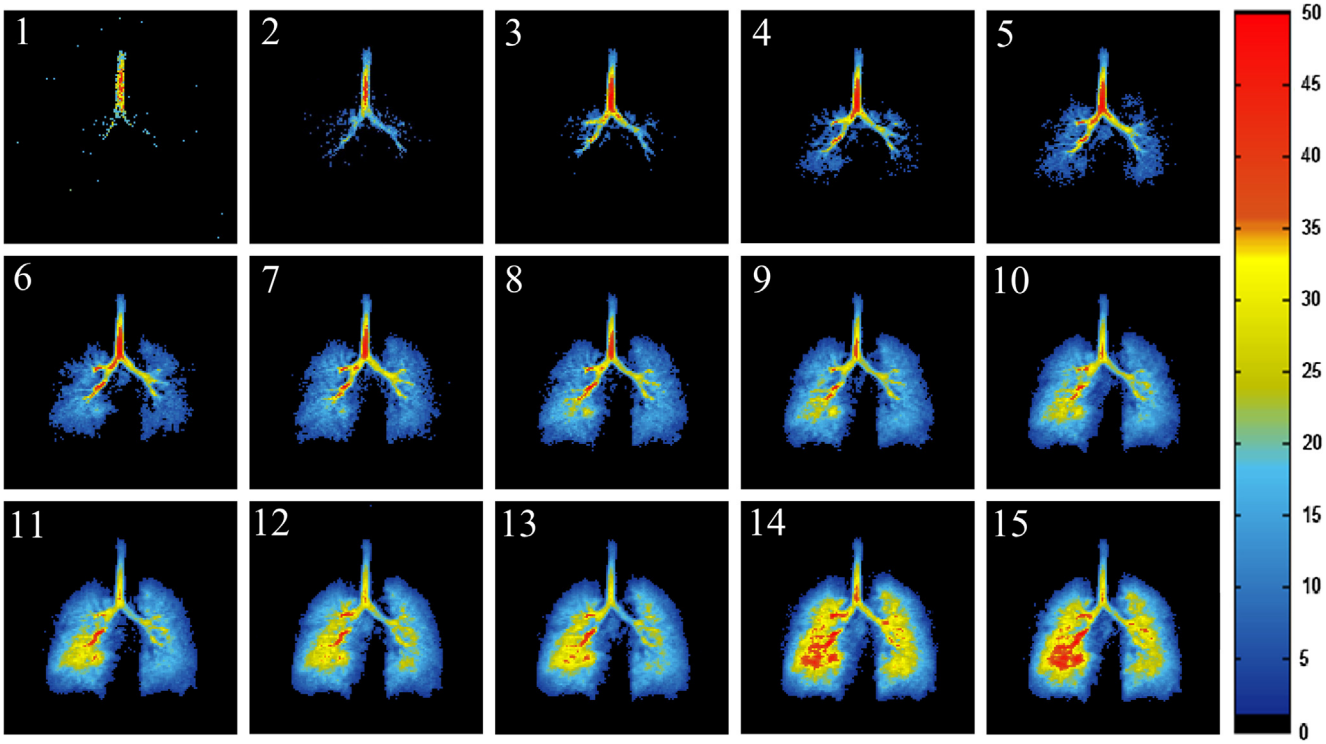


**Fig. 6.** 15 frames of *in vivo* dynamic HP $^{129}$Xe MR images of a healthy volunteer obtained using the proposed method.

bronchi and peripheral lungs with high temporal resolution and minimal artifacts.

Some widely used algorithms (SRCS, L + S) are adopted for comparison. Representative results (14th frame of the reconstructed images) are shown in Fig. 7a–c. Obvious artifacts can be seen in Fig. 7a and b (indicated by white and red arrows). These artifacts are significantly suppressed in the reconstructed image using the L + S + G algorithm, and images show enhanced details. As shown in Table 3, the CNR values of images using the L + S + G algorithm have a statistically significant improvement (more than 30%) com-

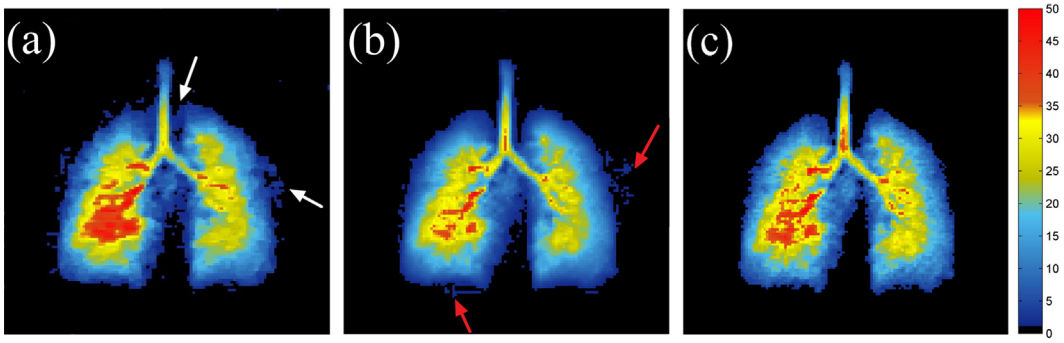


**Fig. 7.** The 14th frame of *in vivo* dynamic HP $^{129}$Xe MR images reconstructed using (a) the SRCS, (b) L + S and (c) L + S + G algorithms.

**Table 3**
Comparisons of CNR values obtained using the SRCS, L + S and L + S + G algorithms for *in vivo* experiments (*I* denotes the improvement of L + S + G algorithm compared with other two classic reconstruction algorithms).

| Subject No. | 1 | 2 | 3 | 4 | 5 | 6 |
|---|---|---|---|---|---|---|
| SRCS | 31.91 ± 9.97 | 34.16 ± 9.01 | 46.47 ± 11.91 | 36.71 ± 13.09 | 30.75 ± 7.56 | 35.86 ± 9.07 |
| L + S | 36.56 ± 9.72 | 34.63 ± 8.31 | 44.50 ± 11.29 | 38.33 ± 9.42 | 34.99 ± 8.44 | 36.87 ± 8.21 |
| L + S+G | 49.68 ± 14.16 | 46.10 ± 12.26 | 59.87 ± 16.30 | 52.75 ± 15.06 | 49.83 ± 12.49 | 49.15 ± 12.88 |
| $P_{L+S+G\_vs\_SRCS}$ | <0.0001 | <0.0001 | <0.0001 | <0.0001 | <0.0001 | <0.0001 |
| $I_{L+S+G\_vs\_SRCS}$ | 55.67% | 34.95% | 28.82% | 43.68% | 62.08% | 37.06% |
| $P_{L+S+G\_vs\_L+S}$ | <0.0001 | <0.0001 | <0.0001 | <0.0001 | <0.0001 | <0.0001 |
| $I_{L+S+G\_vs\_L+S}$ | 35.88% | 33.12% | 34.52% | 37.64% | 42.41% | 33.32% |

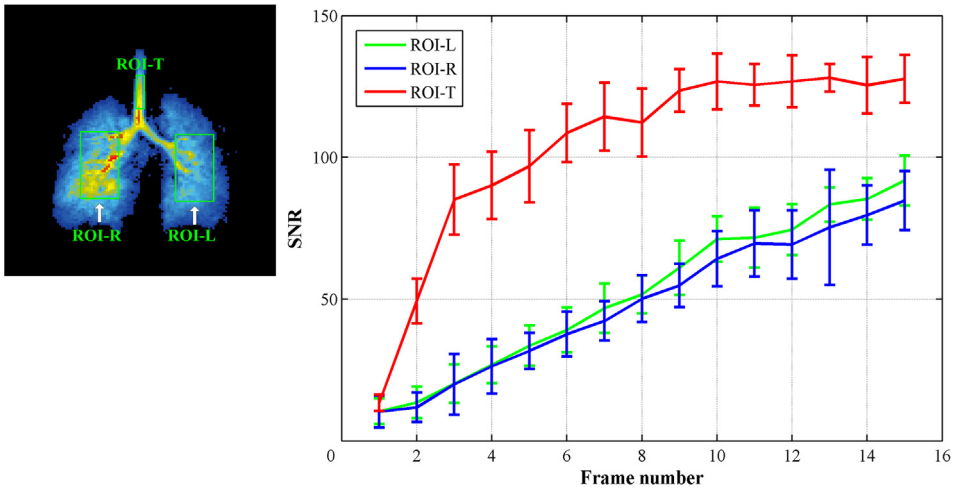


**Fig. 8.** Signal-frame curves of ROIs from the left lung (ROI-L) and right lung (ROI-R) and trachea (ROI-T).

**Table 4**
Spearman's rho values that measure the correlations between the signal-frame curves of ROI-L and ROI-R in six healthy subjects.

| Subject No. | 1 | 2 | 3 | 4 | 5 | 6 |
|---|---|---|---|---|---|---|
| Spearman's Rho Values | 0.985 | 0.943 | 0.979 | 0.932 | 0.970 | 0.958 |

pared with SRCS ($P < 0.05$) and L + S ($P < 0.05$). These experimental results demonstrate the efficacy and robustness of the proposed algorithm.

The signal-frame curves from regions of interest (ROI) of mid zones of the left (ROI-L) and right lung (ROI-R) and the trachea (ROI-T) are shown in Fig. 8. It can be seen that the amplitude ROI-T curve is higher than that of other ROIs and reaches a steady state in a much shorter time. In addition, Spearman's rho values are calculated to evaluate the correlations between signal-frame curves from ROI-L and ROI-R. As demonstrated in Table 4, a strong correlation is observed between the ROI-L and ROI-R for all six healthy subjects. These characteristics of signal-frame curves are consistent with the previously reported results [30].

## 4. Discussion

In this work, a new method is developed to acquire pulmonary dynamic HP $^{129}$Xe MR images with high quality and temporal-spatial resolution. In data acquisition process with undersampling

strategy, a new VFA scheme considering the gas-inflow effects is designed to compensate for the HP longitudinal magnetization decay. After that, an effective reconstruction algorithm constraining the low-rank, sparse and gas-inflow effects is proposed to reconstruct images, aiming to guarantee the image quality.

In the experiments, the proposed method can acquire dynamic HP $^{129}$Xe MR images with the spatial resolution of 3 mm and temporal resolution of 0.44 s, which is superior to the state-of-art pulmonary dynamic HP $^{129}$Xe MRI [30]. High image quality is also achieved, indicated by MAE, SSIM, QILV, CNR and visual effects. The CNR acquired in the experiments *in vivo* is about 50, providing a high quality of the contrast for analyzing lung physiology. This demonstrates the feasibility and effectiveness of the proposed method. Moreover, similar results (CNR and signal-frame curves) of six subjects are acquired, which indicate the robustness of the proposed method.

By maintaining a constant ASI over multiple frames, the proposed VFA scheme effectively preserves the details of the dynamic HP $^{129}$Xe images. This avoids the unfavorable effects of the k-space filtering. As can be seen in the results of conventional VFA scheme, the image noise is serious due to the higher weight of the high frequency part than the low frequency part in the k-space. Similarly, owing to the higher weight of the low frequency part, some details are missing in the results of the CFA scheme. In addition, the new VFA scheme has a good effect in image reconstruction compared with conventional VFA and CFA schemes. This is because that the proposed scheme takes regional gas-inflow effects into account, which is consistent with the proposed reconstruction algorithm. Moreover, maintaining a constant ASI over multiple frames is helpful to acquire more accurate signal-frame curves by considering the gas-inflow effects. Although the application needs a constant gas inflow, we solve it by training all subjects to breathe in the HP $^{129}$Xe gas at a constant rate. In most of the experiments, subjects have good performances in gas inhalation, which are indicated by the reconstructed images. In the future study, a ventilator for humans will be built to achieve a more precise control of inhalation speed.

As for the L + S + G algorithm, it has a significant improvement in the reconstruction quality compared with the SRCS and L + S algorithms. Additionally, the L + S + G algorithm shows a better performance in artifact reduction and detail preservation, which demonstrates the contribution of the incorporation of gas-inflow effects. The second term of the proposed objective function addresses the gas-inflow effects such as the regional increase of the signal until a steady state is reached and the expansion of regions with inhalation. Obviously, most artifacts do not comply with such requirements due to randomness. In this way, these artifacts are removed and the residual artifacts are eliminated by the low-rank and sparse constraints without degrading the image quality. It is also worth noting that the L + S algorithm has a better performance than the SRCS algorithm in most experimental results of this work, which is consistent with the results of previous work [28]. This demonstrates the importance of low-rank and sparse constraints in the image reconstruction.

Our work has several limitations. Due to the AF of 3, the temporal and spatial resolution of FS images acquired in simulation experiments cannot be the same as *in vivo* experiments. Although the matrix size of simulation experiments is set to $64 \times 64$ with respect to the visual effect, the difference between the simulation and *in vivo* experiments cannot be eliminated. Additionally, a large slice thickness (20 cm) is adopted to acquire the signal of HP $^{129}$Xe in the whole lung since the movement of gas into or out of the slice will affect the ASI. This may be solved by applying 3D imaging technique [40] to the proposed method in the future.

## 5. Conclusion

To help mitigate the disadvantages owing to the rapid depletion of nonrenewable HP longitudinal magnetization, we have put forth an effective accelerated dynamic HP $^{129}$Xe MRI algorithm considering the low-rank, sparse and gas-inflow effects constraints in this paper. The proposed method adopts a new VFA scheme to compensate for the magnetization decay, and a reconstruction strategy (L + S + G) to guarantee the high quality and temporal-spatial resolution of pulmonary dynamic MR images. The simulation and *in vivo* experimental results have demonstrated the feasibility, effectiveness and robustness of the proposed method. Compared with several baseline methods, the proposed algorithm is able to generate fewer artifacts and noise while preserving a decent temporal-spatial resolution. This will provide high quality information of pulmonary structure and function, which is valuable for the analysis of the lung physiology.

## Acknowledgments

This work was supported by National Natural Science Foundation of China (81625011, 81771917, 81227902), National Key R&D Program of China (2016YFC1304700) and Key Research Program of Frontier Sciences, CAS (QYZDY-SSW-SLH018). XZ acknowledges the support by the National Program for Support of Eminent Professionals (National Program for Support of Top-notch Young Professionals).

## Declarations of Interest

None.

## Appendix A

According to Eqs. (2) and (3), we can get the relationship between the ASI after the $n$-th excitation [viz., $S_p(n)$] and ($n$-1)-th excitation [viz., $S_p(n\text{-}1)$], that is,

$$\begin{aligned} S_p(n) = S_2(n)/V(n) &= \frac{\frac{S_2(n-1)}{\sin\theta_{n-1}}\cdot\cos\theta_{n-1}\cdot\sin\theta_n + \mu\cdot r\cdot \mathrm{TR}\cdot\sin\theta_n}{n\cdot r\cdot \mathrm{TR}} \\ &= \frac{\frac{S_p(n-1)\cdot(n-1)\cdot r\cdot \mathrm{TR}}{\sin\theta_{n-1}}\cdot\cos\theta_{n-1}\cdot\sin\theta_n + \mu\cdot r\cdot \mathrm{TR}\cdot\sin\theta_n}{n\cdot r\cdot \mathrm{TR}} \\ &= \frac{S_p(n-1)\cdot(n-1)\cdot\cos\theta_{n-1}\cdot\sin\theta_n + \mu\cdot\sin\theta_n\cdot\sin\theta_{n-1}}{n\cdot\sin\theta_{n-1}} \end{aligned} \tag{8}$$

If $S_p(n) = S_p(n\text{-}1)$, $n = 2, \ldots, (M/a)\times K$, viz.,

$$S_p(n) = S_p(n-1) = S_p(1) = S_2(1)/V(1) = \frac{\mu\cdot r\cdot \mathrm{TR}\cdot\sin\theta_1}{r\cdot \mathrm{TR}} = \mu\cdot\sin\theta_1, \tag{9}$$

Then, Eq. (8) becomes

$$\begin{aligned} \mu\cdot\sin\theta_1 &= \\ &= \frac{\mu\cdot\sin\theta_1\cdot(n-1)\cdot\cos\theta_{n-1}\cdot\sin\theta_n + \mu\cdot\sin\theta_n\cdot\sin\theta_{n-1}}{n\cdot\sin\theta_{n-1}}, \end{aligned} \tag{10}$$

After that, the relationship between the $\sin\theta_n$ and $\sin\theta_{n\text{-}1}$ can be represented as follows,

$$\sin\theta_n = \frac{n\cdot\sin\theta_1}{(n-1)\cdot\sin\theta_1\cdot A(n)+1}, \text{ where } A(n) = \frac{\cos\theta_{n-1}}{\sin\theta_{n-1}}, \tag{11}$$

Therefore, if the initial flip angle $\theta_1$ is known under a given $n$ (or if the $\theta_n$ is defined), a series of flip angles are determined, that is,

$$\theta_n = \arcsin\left\{\frac{n\cdot\sin\theta_1}{(n-1)\cdot\sin\theta_1\cdot A(n)+1}\right\},\ \text{where } A(n)=\frac{\cos\theta_{n-1}}{\sin\theta_{n-1}}.$$

To effectively utilize the HP magnetization in dynamic imaging, the last flip angle of the proposed scheme is 90°. For example, when the excitation number is 960, the initial flip angle is 2.423488°. However, the precision of flip angle is ± 0.01° in the MRI equipment (Avanto, Siemens Medical Solutions). Therefore, the initial flip angle is set to 2.42°, and then the last flip angle is 31.81°. Similarly, when the excitation number is 626, the initial flip angle is set to 3.00°, and then the last flip angle is 55.33°.

## References


[1] M.S. Albert, G.D. Cates, B. Driehuys, et al., Biological magnetic-resonance-imaging using laser polarized Xe-129, Nature 370 (1994) 199–201.
[2] W. Ruan, J. Zhong, K. Wang, et al., Detection of the mild emphysema by quantification of lung respiratory airways with hyperpolarized xenon diffusion MRI, J. Magn. Reson. Imaging 45 (2017) 879–888.
[3] N.J. Stewart, J. Parra-Robles, J.M. Wild, Finite element modeling of Xe-129 diffusive gas exchange NMR in the human alveoli, J. Magn. Reson. 271 (2016) 21–33.
[4] H. Li, Z. Zhang, X. Zhao, X. Sun, C. Ye, X. Zhou, Quantitative Evaluation of Radiation-induced lung injury with hyperpolarized xenon magnetic resonance, Magn. Reson. Med. 76 (2016) 408–416.
[5] Z. Zhiying, G. Yu, L. Haidong, et al., Quantitative comparison of lung physiological parameters in single and multiple breathhold with hyperpolarized xenon magnetic resonance, Biomed. Phys. Eng. Express 2 (2016) 055013.
[6] H.U. Kauczor, M. Ebert, K.F. Kreitner, et al., Imaging of the lungs using $^3$He MRI: Preliminary clinical experience in 18 patients with and without lung disease, J. Magn. Reson. 7 (1997) 538–543.
[7] B. Driehuys, G.P. Cofer, J. Pollaro, J.B. Mackel, L.W. Hedlund, G.A. Johnson, Imaging alveolar-capillary gas transfer using hyperpolarized Xe-129 MRI, Proc. Natl. Acad. Sci. USA 103 (2006) 18278–18283.
[8] J. Zhong, H. Zhang, W. Ruan, et al., Simultaneous assessment of both lung morphometry and gas exchange function within a single breath-hold by hyperpolarized Xe-129 MRI, NMR Biomed. 30 (2017) e3730.
[9] H. Marshall, M.H. Deppe, J. Parra-Robles, et al., Direct visualisation of collateral ventilation in COPD with hyperpolarised gas MRI, Thorax 67 (2012) 613–617.
[10] D.A. Roberts, R.R. Rizi, D.A. Lipson, et al., Detection and localization of pulmonary air leaks using laser-polarized He-3 MRI, Magn. Reson. Med. 44 (2000) 379–382.
[11] J.R. MacFall, H.C. Charles, R.D. Black, et al., Human lung air spaces: potential for MR imaging with hyperpolarized He-3, Radiology 200 (1996) 553–558.
[12] D.S. Gierada, B. Saam, D. Yablonskiy, J.D. Cooper, S.S. Lefrak, M.S. Conradi, Dynamic echo planar MR imaging of lung ventilation with hyperpolarized $^3$He in normal subjects and patients with severe emphysema, NMR Biomed. 13 (2000) 176–181.
[13] M. Viallon, Y. Berthezene, V. Callot, et al., Dynamic imaging of hyperpolarized $^3$He distribution in rat lungs using interleaved-spiral scans, NMR Biomed. 13 (2000) 207–213.
[14] J.M. Wild, F.C. Horn, G.J. Collier, H. Marshall, Dynamic imaging of lung ventilation and gas flow with hyperpolarized gas MRI, in: F.T. Hane (Ed.), Hyperpolarized and Inert Gas MRI, Academic Press, Boston, 2017, pp. 47–59.
[15] M. Salerno, T.A. Altes, J.R. Brookeman, E.E. de Lange, J.P. Mugler III, Dynamic spiral imaging of the lung using hyper-polarized 3He: preliminary studies in healthy and diseased lungs, Magn. Reson. Med. 46 (2001) 667–677.
[16] G.A. Johnson, G. Cates, X.J. Chen, et al., Dynamics of magnetization in hyperpolarized gas MRI of the lung, Magn. Reson. Med. 38 (1997) 66–71.
[17] D. Dupuich, Y. Berthezene, P.L. Clouet, V. Stupar, E. Canet, Y. Cremillieux, Dynamic 3He imaging for quantification of regional lung ventilation parameters, Magn. Reson. Med. 50 (2003) 777–783.
[18] J.M. Wild, M.N. Paley, L. Kasuboski, et al., Dynamic radial projection MRI of inhaled hyperpolarized $^3$He gas, Magn. Reson. Med. 49 (2003) 991–997.
[19] J.H. Holmes, R.L. O'Halloran, E.K. Brodsky, Y. Jung, W.F. Block, S.B. Fain, 3D hyperpolarized He-3 MRI of ventilation using a multi-echo projection acquisition, Magn. Reson. Med. 59 (2008) 1062–1071.
[20] D.L. Donoho, Compressed sensing, IEEE Trans. Inf. Theory 52 (2006) 1289–1306.
[21] E.J. Candes, T. Tao, Near-optimal signal recovery from random projections: Universal encoding strategies, IEEE Trans. Inf. Theory 52 (2006) 5406–5425.
[22] E.J. Candes, J. Romberg, T. Tao, Robust uncertainty principles: Exact signal reconstruction from highly incomplete frequency information, IEEE Trans. Inf. Theory 52 (2006) 489–509.
[23] M. Lustig, D. Donoho, J.M. Pauly, Sparse MRI: The application of compressed sensing for rapid MR imaging, Magn. Reson. Med. 58 (2007) 1182–1195.
[24] E. Von Harbou, H.T. Fabich, M. Benning, A.B. Tayler, A.J. Sederman, L.F. Gladden, D.J. Holland, Quantitative mapping of chemical compositions with MRI using compressed sensing, J. Magn. Reson. 261 (2015) 27–37.
[25] P. Svehla, K.-V. Nguyen, J.-R. Li, L. Ciobanu, Quantitative DLA-based compressed sensing for T-1-weighted acquisitions, J. Magn. Reson. 281 (2017) 26–30.
[26] C. Chen, Y. Li, L. Axel, J. Huang, Real time dynamic MRI by exploiting spatial and temporal sparsity, Magn. Reson. Imaging 34 (2016) 473–482.
[27] S.G. Lingala, M. Jacob, Blind compressive sensing dynamic MRI, IEEE Trans. Med. Imaging 32 (2013) 1132–1145.
[28] R. Otazo, E. Candes, D.K. Sodickson, Low-rank plus sparse matrix decomposition for accelerated dynamic MRI with separation of background and dynamic components, Magn. Reson. Med. 73 (2015) 1125–1136.
[29] X.J. Chen, M.S. Chawla, L.W. Hedlund, H.E. Moller, J.R. MacFall, G.A. Johnson, MR microscopy of lung airways with hyperpolarized He-3, Magn. Reson. Med. 39 (1998) 79–84.
[30] O. Doganay, T.N. Matin, A. McIntyre, et al., Fast dynamic ventilation MRI of hyperpolarized 129Xe using spiral imaging, Magn. Reson. Med. 79 (2018) 2597–2606.
[31] D.M.L. Lilburn, G.E. Pavlovskaya, T. Meersmann, Perspectives of hyperpolarized noble gas MRI beyond He-3, J. Magn. Reson. 229 (2013) 173–186.
[32] H. Deng, J. Zhong, W. Ruan, et al., Constant-variable flip angles for hyperpolarized media MRI, J. Magn. Reson. 263 (2016) 92–100.
[33] L. Zhao, R. Mulkern, C.H. Tseng, D. Williamson, S. Patz, R. Kraft, R.L. Walsworth, F.A. Jolesz, M.S. Albert, Gradient-echo imaging considerations for hyperpolarized Xe-129 MR, J. Magn. Reson. Series B 113 (1996) 179–183.
[34] K. Nagashima, Optimum pulse flip angles for multi-scan acquisition of hyperpolarized NMR and MRI, J. Magn. Reson. 190 (2008) 183–188.
[35] Y. Xing, G.D. Reed, J.M. Pauly, A.B. Kerr, P.E.Z. Larson, Optimal variable flip angle schemes for dynamic acquisition of exchanging hyperpolarized substrates, J. Magn. Reson. 234 (2013) 75–81.
[36] C.J. Willmott, K. Matsuura, Advantages of the mean absolute error (MAE) over the root mean square error (RMSE) in assessing average model performance, Clim. Res. 30 (2005) 79–82.
[37] Z. Wang, A.C. Bovik, H.R. Sheikh, E.P. Simoncelli, Image quality assessment: From error visibility to structural similarity, IEEE. Trans. Image Proc. 13 (2004) 600–612.
[38] S. Aja-Fernandez, R.S.J. Estepar, C. Alberola-Lopez, C.-F. Westin, Image quality assessment based on local variance, in: Annual International Conference of the IEEE Engineering in Medicine and Biology Society IEEE Engineering in Medicine and Biology Society Annual Conference, 2006, pp. 4815–4818.
[39] M. Welvaert, Y. Rosseel, On the definition of signal-to-noise ratio and contrast-to-noise ratio for fMRI data, PloS One 8 (2013) e77089.
[40] Y.F. Yen, K.F. Han, B.L. Daniel, et al., Dynamic breast MRI with spiral trajectories: 3D versus 2D, J. Magn. Reson. 11 (2000) 351–359.